Characterization and Retuning of Magnetic Resonance-based Through-the-Body Communications

Hirsa Kia[a], Krishna Kant[a,1]

[a]*Department of Computer & Information Sciences, Temple University, Philadelphia, PA 19122, USA*

Abstract

In this paper, we present a comprehensive characterization of magnetic resonance coupling (MRC) based through-the-body (TTB) communications in the context of chronic disease management networks (CDMN). We have demonstrated that MRC propagation through the human body exhibits fundamentally different characteristics compared to air media, revealing several counterintuitive behaviors that deviate substantially from classical near-field predictions. We also characterize the broadcast channel behavior with multiple simultaneous receivers and build an empirical path-loss model that achieves prediction accuracy within 1 dB. Finally, we study the problem of detuning of resonance in MRC in the context of the entire network and propose two retuning solutions to mitigate it. We show that the proposed retuning mechanism can effectively recover nearly all of the reception loss due to detuning. Overall, the proposed methods provide effective solutions to some of the key challenges of realizing intrabody communication networks for addressing the growing global burden of chronic diseases.

Keywords: Chronic Disease Management network, Magnetic Resonance Coupling, through-the-body communications channel, Path-loss, Retuning Resonance, Q-factor

1. Introduction

There is an increasing array of human assistive technologies that require sensing some vital signals and accordingly applying or simply recommending some corrective action. In some cases, it suffices to obtain the signal via an on-body sensor (e.g., EEG, EMG, heart rate, etc.); however, certain chronic illnesses require the implantation of sensors in the body. In other cases, the decision to get the signal in-body vs. on-body may depend on the tradeoffs of the two. Implanted sensors can get a stronger/clearer signal (e.g., EEG/EMG signals), may be less cumbersome for the patient, and more secure, but at the

Email addresses: Hirsa.kia@temple.edu (Hirsa Kia), kkant@temple.edu (Krishna Kant)

cost of invasiveness, potential adverse effects, and impracticality of replacement/adjustment.

Chronic diseases are becoming increasingly prevalent worldwide, driven by several factors including an aging population in developed nations and escalating levels of pollution (air, water, and food) in developing countries [1, 2]. In the United States, nearly 45% of the population, equating to approximately 133 million people, live with at least one chronic illness [3], and this figure is continually rising.

As the risk of multiple chronic conditions rises markedly with advancing age [4], and with the elderly population expected to nearly double by 2050 [5], there is a pressing need for innovative, cost-effective, and personalized approaches to the prevention and management of chronic diseases [6, 7]. One such solution is to create a chronic disease management network (CDMN) composed of multiple sensors around the affected area to collect and fuse the information for deciding corrective action (perhaps via an actuator that delivers a drug or electrical stimulus). Examples of CDMNs include managing overactive bladder conditions through a spinal cord neuro-modulator that is regulated by an implantable pressure sensor for bladder pressure and a micro-electrode-based system for urine volume monitoring [8, 9, 10]; optimizing pacemaker activity by monitoring pH, oxygen levels, respiration, physical activity, and drug infusion [11, 12]; or employing brain-computer interfaces using an implantable micro-electrode array with over 100 channels [13].

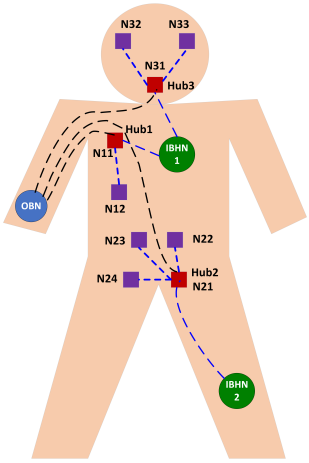

Fig. 1: CDMN illustration

Fig. 1 illustrates a more general CDMN for managing multiple (3 in this case) chronic diseases. For each disease, we expect a *cluster* consisting of a set of sensors connected to a *Hub* node, which collects all the sensor data, makes some local decisions, and potentially has an actuator to deliver a drug/stimulus. We also show an on-body node (OBN) in the form of a smartwatch or similar device, which communicates with the hubs. The OBN is responsible for the overall management of CDMN, a conduit to the outside world (via built-in WiFi or Bluetooth communication ability), and may also serve as a more powerful decision node. The nodes use through-the-body (TTB) wireless communications, which is our key focus in this paper. Since long-lasting batteries are usually too big for implants, a wireless power transfer (WPT) to the nodes is also required and best done by the OBN. For the most part, the WPT and communications face similar issues and thus can use the same technology; therefore, we make no distinction in this paper. We have, however, studied energy transfer and energy efficiency issues in [14, 15]. Fig. 1 also shows "IBHN" nodes or Intra-Body (energy) Harvesting Nodes, which, too, would transfer energy to the needy nodes, but we do not address them specifically.

Since the body can be viewed as a broadcast media, it is essential to coordi-

nate all communications to avoid interference. That is, we need a media access control (MAC) protocol for CDMN. While it might be tempting to use or even propose a sophisticated MAC protocol, we emphasize that (a) the CDMNs are expected to be very small in size, (b) Data transfers in CDMN are very short but happen infrequently (e.g., every few seconds or longer), and (c) Energy efficiency, rather than sophistication, is the most important requirement of CDMN. Thus, the simplest scheme with a known time slot for every communication suffices. We have discussed this aspect (along with some variants to allow for emergency communications) in [15]; however, this paper is not concerned with scheduling issues.

The two most promising technologies include Magnetic Resonance Coupling (MRC) and Ultrasonic Coupling (USC), and our prior experimental work suggests that both work well for TTB communications. Both MRC and USC have been explored in the context of both wearables (on-body) and medical uses (on/in-body), both for communication [16, 17] and WPT [18]. There are currently very few detailed studies of MRC propagation through the body at frequencies of a few to a few tens of MHz range and distances of tens of centimeters, as detailed in section 2.5.

In this paper, we first summarize the MRC body media characteristics and, in the process, provide a clear picture of the unusual characteristics of the body media. We also substantially enhance this characterization by considering the case of a single transmitter and multiple receivers, which we did not consider earlier. Simultaneous reception by multiple receivers is crucial for energy transfer from OBN to implanted nodes and for other broadcast scenarios such as network reconfiguration. It is also nontrivial – connecting multiple receivers exposes the complex interdependencies among them that go beyond the interdependencies in air media due to the conductivity properties of the body. We present both the measurement results with volunteers and an analytic model for attenuation as a function of the number of receivers and their positions on the body. We also conduct a more comprehensive study of the MRC detuning problem. We show, through the example of changes in blood pressure, that the physiological factors can impact MRC tuning. We also examine retuning from the perspective of the entire network rather than a single transmitter-receiver pair.

Abbrv.	**Explanation**
CDMN	Chronic Disease Mgmt. Network
MRC	Magnetic Resonance Coupling
OBN	On-Body Node
USC	Ultrasonic Coupling
TTB	Through-the-Body
NFMI	Near-Field Magnetic Induction

Table 1: List of Abbreviations

The rest of the paper is organized as follows: Section 2 introduces the Magnetic Resonance coupling (MRC) characteristics and detuning problem. In Section 3, the experimental setup and simulation setting are discussed. Section 4 discusses experimental and simulation-based characterization of the TTB MRC communications channel. Section 5 discusses the impact of multiple receivers in/on body receiving signal from a single transmitter. Section 6 details our retuning solution along with the results for the single transmitter-receiver pair. In Section 7, we present

our solutions for the network-wide retuning along with the results. Finally, Section 8 concludes the paper. Table 1 lists some common abbreviations used in the paper.

2. Characteristics of MRC Communications

2.1. MRC Technology and its In-Air Characteristics

Magnetic resonance coupling uses matched transmit and receive antennas, each of which consists of a copper coil in series with a capacitor forming the classical "LC" circuit (where L refers to the inductance of the coil and C refers to the capacitance of the capacitor). The coupling is most effective when the resonance frequency, given by the formula $f_r = 1/(2\pi\sqrt{LC})$, is identical for both transmit and receive coils. Furthermore, to avoid reflections, the two sides also need to have matching complex impedance, which is a function of the L, C, and R (resistance) on each side.

The TTB communications and other applications of MRC assume that the technology works in the *near-field* regime, often under the name NFMI (near field magnetic induction). In contrast, the traditional RF communications, such as BLE, are invariably *far field*. The near-field assumption holds when the operating distance d is much smaller than the wavelength λ_r, or more precisely, $d < \lambda_r/2\pi$ [19]. For example, a popular operational frequency for NFMI is 13.56 MHz, which is the standard frequency for RFID operation. At this frequency, the near-field limit is 3.5m in the air. In the case of far field, i.e., when $d \gg \lambda_r/2\pi$, the coupling is no longer magnetic; instead, the signal travels through radiative means. The traditional RF technologies operate at much higher frequencies and are thus necessarily far-field at distances of interest. In particular, RF power is transferred through Friis equation for propagating EM waves, where electric and magnetic fields are coupled through Faraday's and Ampere's laws in Maxwell's equations. The concept of near-field is really an idealization and is characterized by making some assumptions that effectively decouple the magnetic and electric fields.

The resonant LC circuit in MRC produces a magnetic field that induces current flow in the receiver coil. *In the air media*, the received power is related to the transmitted power using Lenz Law [19]. This relationship suggests several key characteristics for the communication channel. The induced current increases linearly with the operating frequency and goes down very rapidly with distance h (as h^{-3}). Since the power is proportional to I_r^2, the induced power decays as h^{-6}, which is much faster than the decay for the far-field (or RF) case, where the power goes down as h^{-2}. The very rapid decay of the induced power with distance makes the MI technology inherently a small range technology, and this effect is usually more limiting than the near field requirement of $h < \lambda_r/(2\pi)$. The area of transmit and receive coils (proportional to ρ_t^2 and ρ_r^2 respectively) and the number of turns (K_t and K_r) directly influence the mutual inductance and hence the induced current. Increasing the range requires bigger coils and more turns, both of which may be undesirable in applications where

a small size is required. The frequency and the transmit coil current directly increase the induced current, and hence the overall range, but at the cost of higher power consumption. Lenz's law also predicts that the received power decays as the cosine of the angle between the transmit and receive coils; that is, for maximum energy transfer, the two coils should be facing each other, and no power will be received if the two coils are at a 90-degree angle. We show in section 2.3 that many of these properties do not hold in the body media.

2.2. Fundamentals of MRC

MRC works by energy transfer between a transmit and a receive coils of inductance L in series (or parallel) with capacitance C. At any angular frequency $\omega = 2\pi f$ (with frequency f), such a circuit has capacitive and inductive reactances, denoted X_L and X_C respectively, given by $X_L = j\omega$ and $X_C = -1/(j\omega)$. The total impedance of a series RLC circuit is given by

$$Z = R + j\left(X_L - X_c\right) = R + j\left(\omega L - \frac{1}{\omega C}\right) \tag{1}$$

When $X_L > X_C$ the circuit is *inductive*, whereas $X_C > X_L$ makes the circuit *capacitive*. Electrical resonance occurs when the inductive and capacitive reactance are equal,

$$X_L = X_c, \quad \implies \omega_r L = \frac{1}{\omega_r C}, \quad \implies \omega_r = \frac{1}{\sqrt{LC}} \tag{2}$$

which implies that $\omega_r = \frac{1}{\sqrt{LC}}$. In a resonant condition, the impedance of the circuit becomes purely resistive, i.e., $Z = R$.

An important performance indicator of an RLC circuit is the *quality factor* Q, defined as the ratio of the energy stored in the circuit to the energy dissipated by the circuit [20, 21]. It is merely the ratio of reactance and resistance, and is given by $Q = \frac{1}{\omega_r RC}$.

$$\begin{aligned} Q &= \frac{\text{Energy stored in the circuit per cycle}}{\text{Energy dissipated by the circuit per cycle}} \\ &= \frac{\text{Reactance}}{\text{Resistance}} = \frac{X_L\,(\text{or } \mathrm{X_C})}{R} = \frac{\omega_r L}{R} = \frac{1}{R\omega_r C} \end{aligned} \tag{3}$$

The quality factor mainly indicates how efficiently inductors and capacitors in the circuit transfer their energy from the source to the load. It can also be defined as the frequency-to-bandwidth ratio of the resonator, i.e.

$$Q = \frac{f_r}{\Delta f} = \frac{\omega_r}{\Delta\omega} \tag{4}$$

where Δf is the resonance width, i.e., the bandwidth over which the power is greater than half the power at the resonant frequency. $\Delta\omega$ is the corresponding angular half-power bandwidth (See Fig. 2).

The transmit coil can transfer energy to the receive coil because of the mutual inductance between the two coils, denoted M. Thus, a time-varying voltage V_1 (and corresponding current I_1) in the transmit coil induces a current I_2 in the receiving coil. If the resistor, inductor, and capacitor values of the two coils are (R_1, L_1, C_1) and (R_2, L_2, C_2) respectively, then from Kirchoff's laws, it is easy to conclude that $I_2 = -\frac{j\omega_r M}{R_2} I_1$.

Thus, if the transmitted data is modulated on the magnetic flux, then the receiver can receive and demodulate the signal. The effectiveness of the mutual coupling is measured by the *coupling coefficient* κ, which can be estimated as

$$\kappa = \frac{M}{\sqrt{L_1 L_2}} \tag{5}$$

If P_1 and P_2 are the transmitted and received power, respectively, then the power transfer ratio is given by [21]

$$\frac{P_2}{P_1} = \frac{\omega_r^2 M^2 R_1 R_2}{R_1^2 R_2^2} = \kappa^2 Q_1.Q_2 \tag{6}$$

where Q_1 and Q_2 are the quality factors of the transmit and receive coils, respectively. Thus, the power transfer is proportional to the coupling coefficient and the quality factors of the transceiver coils [22]. It is clear that to have the perfect energy transfer, the coupling factor κ needs to be equal to $\frac{1}{\sqrt{Q_1 \cdot Q_2}}$. This coupling factor was used in the circuit simulations.

2.3. Unique Properties of Body Media for MRC

Unfortunately, most of the above-mentioned and well-understood properties of MRC (or NFMI) falter in a highly complex environment like the human body, and we end up with many surprising and nonintuitive behaviors, which have motivated our prior work on the topic [23, 24] and the extensions described here.

The most important aspect of non-air media is its electrical permittivity ϵ_m and magnetic permeability μ_m. These affect the speed of EM propagation, denoted by c_m, through the media. In particular, $c_m = c_0/\sqrt{\epsilon_{rm} \times \mu_{rm}}$, where c_0 is the "speed of light" through the vacuum, and ϵ_{rm} and μ_{rm} are the electrical permittivity and magnetic permeability through the media relative values to the values in vacuum ($\epsilon_0 = 8.854e{-}12$ and $\mu_0 = 4\pi \times 10^{-7}$). Note that by definition, $c_m = \lambda_m \times f$ for wavelength λ_m and f_m as frequency. Thus, a high permittivity or permeability reduces both λ_m and c_m at a given frequency.

For the human body, $\mu_{rm} \approx 1$ but ϵ_{rm} varies tremendously from organ to organ [25, 26], with absolute values (including real and imaginary parts) ranging from tens to thousands. The imaginary part results from the conductivity of various organs, which also varies significantly. Furthermore, the permittivity is not constant but goes down with the operating frequency. Table 2 shows a sample of relative permittivity and conductivity at both 13.56 MHz and 25 MHz, and one can see significant variations even within a single organ.

Table 2: Relative Permittivity and Electrical Conductivity of Various Tissues at Different Frequencies[27]

Tissue type	**13.56MHz**		**25MHz**	
	Rel. Permit.	Elec. Cond.	Rel. Permit.	Elec. Cond.
Blood	210.6	1.12	133.1	1.15
Muscle	138.4	0.63	99.3	0.65
Skin (dry)	285.2	0.24	175.7	0.32
Fat (avg.)	25.4	0.06	18.6	0.06

These numbers have many implications in terms of channel characteristics, which make the human body completely different from air. First, the average relative permittivity within the body is of the order of 100, which implies that the wavelength at a given frequency would be around 1/10th. It further implies that the near-field limit would also be 1/10th; e.g., around 35 cm at 13.56 MHz, rather than the 3.5m in air. Thus, the propagation inside the body would operate in the "mid-field" rather than near-field, which implies far more complex characteristics than Lenz's law for near-field would suggest.

The second issue is conductivity – a fairly high conductivity means that the propagation within the body is somewhere in between the current flow through a conductor, magnetic induction, and EM wave propagation, and the behavior strongly depends on the frequency. Added to this is the third issue: the extreme heterogeneity of the body media. It is well known that when EM waves encounter a boundary with dissimilar electromagnetic properties, they will undergo some refraction, reflection, and dispersion. Although difficult to characterize precisely, the impact of numerous dissimilar boundaries inside the body is scattering, essentially amounting to isotropic propagation. This is borne out by the lack of sensitivity of attenuation to the relative orientation of the transmit and receive coils, which is quite helpful in the intrabody network context. There are other unusual behaviors as well, as we discuss later in the paper.

2.4. Parameter Drift and Retuning of MRC

It is clear that to maximize energy transfer, both Q_1 and Q_2 should be as high as possible. Unfortunately, a high Q value results in a much sharper peak in the resonance curve as shown in Fig. 2. The key problem with the sharp peak is its stability, since a slight change in the parameters or load variations can change the resonance frequency enough to substantially lower the transfer efficiency. Since the implanted nodes in CDMN should be able to work well throughout the lifetime of the patient, *we need an automated mechanism to retune the network to maintain a near-optimal level in spite of the drift/changes in the resonance peak.*

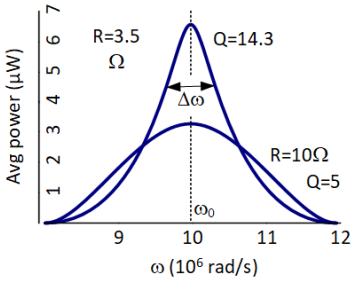

Fig. 2: Resonance Illustration

In general, there could be multiple reasons for drift/changes, some significant, some not. For example, the drift in the capacitance due to aging and

temperature variations in the class 1 CoG capacitor used in medical applications is generally quite small or negligible [28]. Similarly, the coil inductance is unlikely to drift over time. However, the mounting of the capacitor/inductor on the circuit board and the solder can experience changes over time, particularly at higher temperatures [29]. Although in rare cases the circuit may fail, we focus only on drift, which is much more likely.

In addition to the potential drift in the resonance circuit itself, there are other changes whose impact could perturb the resonance significantly. One source of perturbation is the slow shift in the node location in the body. Although slight movements and orientation changes occur all the time within the body, there could also be a longer-term drift as the patient ages. These changes would also change the parasitic capacitance contributed by the body and its contact with the coils. Another potential source of perturbation concerns the change in physiological parameters of the person. Some of these could vary rather frequently (e.g., blood pressure, heart rate, skin conductance, etc.) and are best ignored as they are transient. However, there could also be longer-term changes as well in many parameters, including blood pressure, fat, muscle, bone density, etc. The changes could lead to higher or lower signal attenuation than the nominal value. In the former case, retuning is crucial from an energy transfer perspective and may be important for communication over longer TTB distances. In the latter case, no retuning can help lower the transmit energy.

2.5. Related Work

2.5.1. BioMedical Use of MRC and USC

The biomedical applications of MRC and USC generally consider very short distances (a few mm to a few centimeters). Foundational MRC work by Kurs et al. [30] introduced strongly coupled magnetic resonance for mid-range WPT, later adapted for biomedical use by Kiani et al. [31], who optimized a three-coil system for efficient powering of implants. Ho et al. [32] demonstrated midfield powering of a millimeter-scale cardiac implant at over 5 cm depth. More recently, flexible and compact MRC coil designs have emerged: Xu et al. [33] proposed a 3D dual-coil system achieving 70 mW at 6 mm with 35% efficiency, while Hoang et al. [34] showed that resonator coils at 6.78 MHz maintain 60-75% efficiency even when bent. A triple-layer 13.56 MHz coil architecture further pushed efficiency to 88% at 10 mm [35]. Kouhalvandi et al. [36] surveyed design trade-offs for MRC systems in biomedical contexts. Ozeri and Shmilovitz [37] pioneered ultrasonic transcutaneous energy transfer (UTET) to power implants several centimeters deep. Kim et al. [38] explore an USC-powered microprobe for electrolyte ablation. Chang et al. [39] develop a USC power receiver for medical devices and discuss MRC power transfer to medical devices. Seo et al. [40] introduced "neural dust," a batteryless, sub-mm implant platform powered and read via ultrasonic backscatter, enabling in vivo neural recordings. Weber et al. [41] and Charthad et al.[42] extended this concept to pressure sensors and neurostimulators using time-multiplexed ultrasonic power and data links. Wang et al. [43] recently demonstrated a fully implantable ultrasonic deep brain stimulator using dual-frequency lead-free piezoelectric harvesters.

2.5.2. Characterization of Body Communications Media

Much of the longer-range characterization models the body either separately for different types of tissues, or by using average dielectric properties, or in the context of very high frequencies. Ibrahim et al. [44], for example, explore both through COMSOL simulation of EM propagation through a homogeneous soft-tissue media and via some experiments on chicken breast. It studies power transmission efficiency (PTE) and power delivered to the load (PDL) for MRC and USC implant of two different sizes, with mixed results. They did, however, find that the USC link is more sensitive to Rx misalignments and orientations than MRC. Wen et al. [17] is typical of channel characterization efforts through measurements and simulations. It considers propagation over a much higher frequency region (50 MHz to 2.4 GHz) and uses average dielectric properties of the human body, which is not appropriate at lower frequencies. It studies ear-to-ear MRC transmission and finds that it works best in the 100-200 MHz range.

Although wireless power transfer (WPT) through the body has been explored extensively, the literature only speaks of WPT to a single node rather than a network. For example, MRC is considered in [45, 46, 47], ultrasound in [48] and comparison between various techniques [49, 22].

2.5.3. MRC Returning Problem

The problem of MRC detuning has been considered in the literature; however, the retuning solutions invariably use a switchable capacitor/inductor matrix, which makes them rather heavy-duty. For example, Si et. al. [50] consider power transfer to a pacemaker from outside and use both capacitor switching and frequency switching to control power transfer. Lim et al. [51] introduce a self-adaptive capacitor matrix with automated searching for a configuration by changing the distance between transmit and receive coils. Another method is to adjust the capacitance via pulse-width modulation (PWM) of the input signal. This controls how much chance the capacitor gets to charge/discharge in each cycle, which effectively changes its capacitance. Porto et al. [52] do this by using an amplifier, and a double-sided version is discussed in [53]. PWM is unworkable in our context because of potential disruption to communication in the integrated power transfer and communications. A better method is to change the capacitance directly using the widely available voltage voltage-controlled capacitors with built-in push-pull circuit [54]. In all cases, the time required to complete the change must be respected, and it would introduce some delay in the communications and WPT.

The capacitance change can be used to counter the drift by ensuring that the operating frequency is restored back to the resonant frequency. This is a popular method explored in several papers; for example, a self-oscillating switching technique was used in [55]. Unfortunately, frequency switching is not only complex in our context (as discussed later) but also requires the receiver to re-latch to the changed frequency to enable proper communication. Another method is to control the phase shift on the receive side by using the semiactive rectifier (SAR). The trigger modes of the driving signals of SAR are altered to

achieve matching of the load resistance or reactance. Mai et al. [56] use both pulse width and the phase shift angle control to provide matching for both the drift and load resistance variations. In our context, the rectification will work only for WPT, not communications.

2.5.4. MRC vs. USC for TTB Communications

Given the popularity of USC in biomedical applications, our prior in [57] has evaluated USC both experimentally (via on-body experiments) and via Sim4Life simulations using its acoustics package. We generally found that USC has a somewhat longer range than MRC, and like MRC, the results are quite different than what one would expect in the air. In particular, contrary to expectations, the path-loss goes down with frequency, which led us to try higher frequencies in multi-MHz range. Unfortunately, the flat diaphragm USC transducer that we used (to compare directly with the flat MRC coil) must necessarily become thinner as the frequency increases [58]. This limited the actual experiments to only 8 MHz. However, like MRC, we found an excellent match between experiments and Sim4Life simulations and thus explored higher frequencies via simulation. The range advantage of USC mostly disappears beyond the 13.5 MHz range. Also, acoustic impedance matching could be difficult [39] and hence we primarily focus on MRC in this paper.

2.5.5. Our Prior Work and Relationship to This Paper

We have explored MRC (and to a limited extent USC) for the body media in our prior work. In particular, we conducted experiments with several volunteers and measured attenuation as a function of distance in [23] and found that the attenuation increases rather slowly with distance. We also experimented with several variations, such as the position of antennas on the body, coil orientations, subject movement/posture-change, etc., and found that the MRC propagation through the body is quite stable. We have also studied the packet delivery ratio at different distances in [24]. We explored the simulation of MRC in [59] and found that the simulation results match measurements quite well. Preliminary work on MRC retuning for a single transmitter-receiver pair is discussed in [60]. We have explored some of the energy transfer issues in [14] and communications issues in [15]. This paper extends our prior work by: (1) developing a comprehensive path-loss model for multi-receiver MRC scenarios, addressing the gap in understanding broadcast energy delivery, and (2) introducing network-wide retuning strategies using a rectified error measure that prevent destructive interference between controllers. While our previous studies established the feasibility of MRC for intrabody networks, this work provides the essential modeling and control mechanisms needed for the practical deployment of battery-less implanted device networks.

3. Experimental Characterization of Body MRC Channel

3.1. Antenna Designs for Experiments

Because of the infeasibility of conducting any in-body experiments, results reported here rely on either on-body experiments or on simulations[1]. For real experiments, flat 20 mm diameter coils (like the one in Fig. 3(b)) are attached to the volunteer's skin at the desired position using electrical gel and covered with magnetic shielding to avoid in-air leakage.

We designed several RLC circuits focusing on the resonance frequency of 13.56 MHz for the experiments. The parameter values for the RLC circuit are shown in Fig. 3(a). To conduct retuning experiments, we also needed to build circuits with different parameters as well. A simple solution for this is to use mechanically variable inductors and capacitors (usually changed by turning a screw) and (de)tune them manually as needed. However, such variable inductors/capacitors are notoriously unstable to the point of being unusable for small drifts that we are interested in. The voltage-controlled inductors and current-controlled capacitors require more complex circuit design, and obtaining high-precision components is difficult. Therefore, we built LC circuits with suitably chosen capacitor values along with a change in the number of turns to change the inductance (Changing coil diameter requires different coils, which were not available). Note that the resistors and capacitors come only in certain well-known sizes and have 1% or worse tolerance; therefore, the practical problem of achieving the precise resonance frequency or matching the transmitter and receiver is quite tricky to solve and very time-consuming. We largely achieved this by trial and error.

Parameter	**Value**
Inductance	9.27 μ H
Capacitance	14.86 pf
Resistance	50 Ω
Coupling (k_{mrc})	0.063

Fig. 3: (a) Circuit parameters, (b) A sample MRC Antenna

There are other challenges also brought about by using the antenna on-body. The human body has a small capacitance that must be accounted for in achieving the precise resonance frequency, although this appears to remain constant. Other issues concern the quality of antenna contact with the skin, signal leakage outside the body, and the impact of the skin properties of the person. For good contact, we used an electric gel, and we covered the transmitter and receiver with a magnetic shield to avoid leakage outside the body and ensure that only the TTB communication path is used. Although skin resistance is a function of many parameters (e.g., skin type, hydration, temperature, stress level, etc. [61]), the impacts on overall communication were not deemed to be substantial.

[1]Human experiments were done under the approved IRB protocol #28089

3.2. Design of On-Body Human Experiments

For our experiments, we asked the volunteer to either sit in a chair or stand on the lab floor. Neither mattered since the lab floor is nonconducting. We also confirmed that different postures (e.g., seated on a cushioned chair with feet off the ground) did not make any difference. We measured the communication performance in two ways. First, we connected the transmitter to a signal generator and receiver to a vector network analyzer (VNA) to measure the received signal. There was no common ground connection between the signal generator and the VNA, as that would invalidate the results.

For real packet transmissions, we used a pair of USRP (Universal Software Radio Peripheral) N210 boards produced by Ettus Research [62]. The boards enable flexible implementation of software radio, including various types of modulation schemes, along with the ability to connect different types of antennas. It includes a Xilinx® Spartan® 3A-DSP 3400 FPGA, 100 MS/s dual ADC, 400 MS/s dual DAC, and Gigabit Ethernet connectivity to stream data to and from host processors. A modular design allows the USRP N210 to operate from DC to 6 GHz. In our experiments, we used BPSK modulation to study the packet delivery ratio through the body at different distances.

3.3. Sim4Life Simulation Based Evaluation

Because of the limitations of conducting real communications experiments in the body media, a detailed simulation of electromagnetic activity within the human body is an important technique to obtain insights. This amounts to solving Maxwell's equations in a complex body media. There are several open source simulation packages summarized in [63], but most do not come with human phantom models. Two packages that do include them are CST Studio (open source) and Sim4Life (commercial) [64]. Sim4life supports very detailed "Virtual Population" (ViP) phantom models of the human body, including all of the organs.

Realistic modeling of EM propagation through the human body requires accurate handling of surfaces with very different EM properties; therefore, numerical solutions using a fine 3D grid ("voxel") are necessary. Small voxel size increases simulation time substantially, but is essential to obtain acceptable accuracies.

The three main methods in this regard are [63]: Finite-differences-time domain (FDTD), Finite Element Method (FEM), and Method of Moments (MoM), or equivalently, Boundary Element Method (BEM). We have used Sim4Life FDTD method in our modeling. Most results were obtained by making the quasi-static assumption appropriate for NFMI. These tend to be far less resource-intensive than solving full Maxwell's equations, which would be more accurate at higher frequencies; however, the main reason to stick with quasi-static assumption is the rather poor numerical properties of the full FDTD solvers in Sim4Life at low frequencies. All of the work in the literature using a full FDTD solution that we are aware of assumes Gigahertz frequencies; the methods become rather unstable in the 10 MHz range that we are interested in.

We use the "Duke" model in Sim4Life, an MRI-based full-body model obtained from a virtual population. The model was segmented into 75 anatomical body tissues/organs, with a resolution of $1.5 \times 1.5 \times 1.5\ mm^3$ throughout the body. The height and weight of the model were 1.77 m and 70.2 kg, respectively. Since a FEM solver is capable of operating at various frequencies, we obtained the path-loss distribution with the human body model using the magneto FEM vector-potential.

4. Results on MRC Body Channel Characterization

In this section, we show that the Sim4Life simulation results match experimental results extremely well and then report some additional simulation-based results that show the very peculiar behavior of the MRC body channel. We also show some experimental results on the impact of physiological parameters on MRC resonance, which is important from the perspective of short-term retuning of the circuits.

4.1. Impact of Physiological Parameters on MRC Channel

In the following, we show the impact of two physiological aspects of the body that tend to fluctuate a lot. The first is body (skin) temperature, which varies both normally and as a result of sickness. The second is blood pressure, which is affected by numerous factors such as exercise, stress, disease, age, etc., and is often closely related to the heart rate. In terms of MRC retuning, while there is little point in chasing the very short-term changes, longer term chances (e.g., age/sickness-related) can make the CDMN more robust.

4.1.1. Skin Temperature vs. Transmission Efficiency

We examine the path-loss with respect to the skin temperature. For this, we artificially increased and decreased skin temperature in the left arm and measured the path-loss. A common rubber bottle was used as the heating/cooling agent. The bottle was placed on the arm, between the two sensors, removed after 2 minutes to avoid any extended impacts, and then the received power was measured. The experiments were done at 5 different temperatures, 10°, 15°, 27°, 35° and 40° Celsius. As can be seen in Fig. 4.a, there is less than 1.78 dB loss between maximum and minimum measured dB loss, and no apparent correlation between the temperature and efficiency is observed.

Table 3: Impact of Skin Temperature on Pathloss

Temp. (°)	Pathloss (dB)
10	16.60
15	16.14
27	16.31
35	14.91
40	16.69

4.1.2. Blood Pressure vs. Transmission Efficiency

In the second experiment, we measured the blood pressure (both Diastolic and Systolic) and path-loss. The measurements were done at different times of the day and after different activities, resulting in a range of numbers for BP. As can be seen in Fig. 4.b, there is approximately 8 dB difference between the

maximum and minimum measured dB loss, and it changes rather substantially. Although our experiments do not show a very clean relationship between BP and path-loss, we can see that blood pressure and possibly other body parameters affect how efficient the transmission is. Therefore, it is important to compensate for such changes automatically to keep the transmission efficiency high. The proposed control scheme attempts to address the need for adaptation in such scenarios.

4.2. Comparison Between Experimental and Simulation Results

The Sim4Life model was run for the same (on-body) locations of transmitter and receiver as in the real experiments to enable a direct comparison. Nevertheless, it is important to note that the Duke model in Sim4Life does not correspond to the characteristics of the subject used for experimentation. Nevertheless, the impact of individual differences should be rather small, as suggested by our prior work in [23].

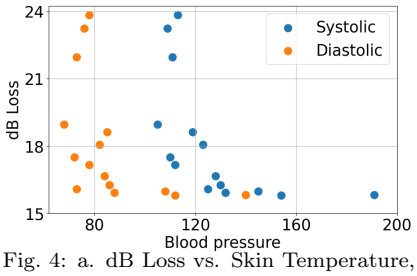

Fig. 4: a. dB Loss vs. Skin Temperature, b. dB Loss vs. Blood Pressure

Fig. 5 shows the comparison for a wide range of frequencies from 3 MHz to 50 MHz. It can be seen that in most cases, there is a very good match between the two. In all cases, the measured loss is larger than the simulated one, which could be explained by the fact that the simulated situation is ideal (simulation has no notion of skin-contact quality, field leakage outside the body, or the minor loss of signal between the measuring equipment and the measured signal on the body). Accounting for this will perhaps show an even better match. We found such a match in all the other (unreported) cases as well. The somewhat variable difference between measured and simulated values can be attributed to various sources of variations including: (a) body-type of the volunteer vs. that of the phantom, and (b) difficulties and practical issues in setting the precise values of L and C in each case, as mentioned in section 3.1, and (c) unmodeled issues in the simulations.

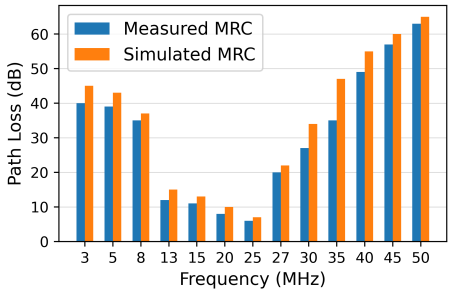

Fig. 5: MRC measured & simulated pathloss vs. freq.

It is worth noting here that both the Sim4Life simulation and real measurements have several potential sources of limitations; thus, a consistent match in the shown (and other results not shown here) provides confidence in the robustness of both simulation and measurements. In particular, Sim4Life is an extremely complex package with numerous parameters, and its solution method for Maxwell's equations using the finite-element method does have numerical and quantization issues. Furthermore, even though the ViP phantom models

are assembled from careful 3D imaging of cadavers, they do not faithfully represent things like flowing blood, beating heart, etc. Real measurements also have several sources of errors, such as potential ground loops, parasitic capacitances, in-air leakage, and measurement errors.

The most interesting result from Fig. 5 is the "sweet-spot" for the frequency, even in a rather limited range of 2-50MHz. In the figure, the path-loss is minimum around 25MHz and increases on both sides. The analytical model for magnetic resonance propagation through the air cannot explain such behavior. We believe that this is partly a result of frequency-dependent permittivity and conductivity as illustrated in Table 2. The frequency at which the minimum occurs depends on several parameters as discussed later, and should not be construed as fixed. Even more significantly, the actual values of path-loss very much depend on the Q-factor of the coils. In Fig. 5, the Q-factor is quite high (210 at 25 MHz), which would lead very sharp resonance peak. Maintaining this peak may be somewhat challenging in the face of short-term fluctuations. If we bring Q down to a more manageable value, the path-loss would increase. Another issue is that the Q-factor will change with frequency because of practical difficulties in maintaining the same L/C ratio. However, the experiments do suggest that the behavior remains intact.

4.3. Further Simulation-Based Characterization of MRC

Given the accuracy of the above simulation results, it is possible to conduct additional investigation into MRC using Sim4Life that wouldn't be possible with human subjects. One important aspect here is the potential difference between in-body vs. on-body placement of the antenna. Fig. 6a shows the comparison of in-body vs. on-body results. For the in-body, the coils were placed in the same spot but under the skin. (No shielding is required since the propagation through the air is not modeled). It is seen that the difference between on-body and in-body scenarios is rather small, with on-body showing a slightly higher path-loss as one might expect.

We further studied the behavior of MRC with frequency when the number of turns of the coil is changed. Fig. 6b shows the behavior of the 20mm coil for 3, 5, and 7 turns. In terms of relative path-loss, the results are as expected – the path-loss decreases with the number of turns. However, there is a slight shift to the left with an increasing number of turns. This behavior has been reported in [65] and is again not expected in a homogeneous media like air.

Given the "sweet-spot" behavior of path-loss vs. frequency, we decided to examine optimal frequency as a function of coil size for MRC. The result is shown in Fig. 6c. It is seen that there is a consistent decrease in optimal frequency as the coil size increases. Please note that these results were obtained by trial-and-error, since there is no equation to indicate the optimal operating point; therefore, the results are approximate. Further approximation errors can be expected due to variation in the Q-factor. To keep the same Q-factor, the ratio of L to C would need to be maintained the same; however, this is difficult to do as explained in section 3.1.

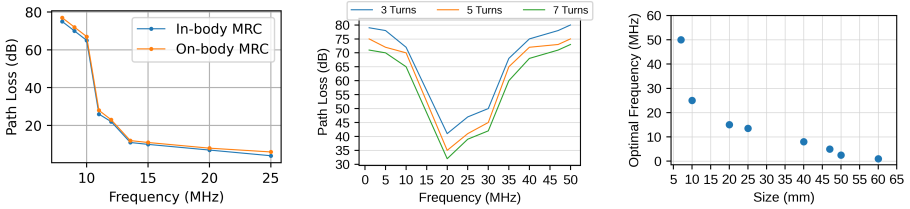

(a) (b) (c)

Fig. 6: (a) MRC simulation result for in-body and on-body cases (b) Simulated path-loss vs. frequency for different # of turns in coil (c) Optimal frequency of operation vs. coil diameter for 7-turn coil

Our exploration suggests that the signal propagation behavior through the human body is quite different than in a homogeneous nonconducting media like air. The results are also markedly different from are often observed with idealized modeling of the body with average dielectric parameters or by considering tissues of only one type. Our results are, however, consistent with those reported in [65] and [66].

5. Modeling Attenuation with Multiple Receivers

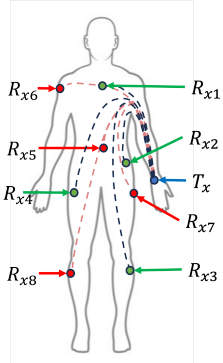

Fig. 7: MR receiver placements

As stated in the introduction, a long-lasting intrabody network should avoid batteries because of the highly invasive procedures needed to change them. Instead, we assume that all intrabody nodes in the network will have a small supercapacitor to store energy, and a mechanism to charge it regularly through an on-body device like a smart watch. The extremely heterogeneous nature of body media implies that it is not possible to make the wireless link between two nodes largely directional, even with a directional antenna. Instead, any energy or message transfer will be received by all of the nodes in the network, although clearly the path-loss would vary. It is thus crucial to study what happens to path-loss in the case of single-transmitter and multiple receivers. In the body media, multiple receivers interact for two reasons: (a) Body has significant conductivity, which means that the induced current in each receiver coil amounts, to an extent, an energy draw, that depletes it for other receivers, and (b) The receive coil locations are not only limited to the rather small area of the body but the sensors related to a specific chronic diseases are generally clustered around a small area, thereby having substantial mutual coupling. The highly heterogeneous body media environment further complicates the picture.

5.1. Multi-Receiver Path-Loss Data Collection

Given the complexities of a multi-receiver environment, we took the approach of conducting a series of multi-receiver experiments on volunteers and then build

an then build an empirical model of path-loss. Conducting these experiments poses practical problems in terms of the number of simultaneous receive coils that we can prepare and place on the volunteer's body and run wires to the network analyzer to collect the data. We created 30 experimental configurations with 8 different positions on the body for the receivers with the transmitter on the wrist. Up to 4 of these 8 locations had a receiver present in these configurations. We henceforth denote the ith receiver location as R_{xi}. All the experiments are done with a 13.56 MHz frequency.

The locations of the receivers in the first set are on chest, left side of the waist (LW), left calf (LC), right thigh (RT), and the receivers in the second set are on placed on right arm (RA), left thigh (LT), right calf (RC) and torso as shown in Fig. 7. The results can be seen in Table 4. The path-loss seem to be related to the on the body distance of the receiver from the transmitter, the distance to the other receivers, the number of receivers, and the location of the other receivers relative to each other, i.e. if receiver A is "behind" the receiver B, then there is a shadowing effect for receiver A. Another observation is that the total path-loss seems not to change much for different cases, especially in the case of multiple receivers.

5.2. Intra-body Path-Loss Model

In order to develop energy delivery strategies for intrabody networks, it is important to create a simple model of path-loss as a function of receiver locations and the number of receivers. Given a specific receiver setup (e.g., single receiver, pair of receivers, etc.), the total path-loss for each receiver i consists of two components:

1. A base path-loss $L_{base}(i)$ in dB that depends on d_i, the in-body distance from the transmitter to the receiver i.
2. Additional loss in dB from interactions of receiver i with other active receivers (if any). We denote the interaction path-loss due to receiver j as $L_{int}(i, j)$.

We adopted this specific functional form to balance physical realism against computational tractability for network optimization. The base path-loss $L_{base}(i)$ follows the familiar power law relationship $(\alpha d_i^{\lambda} + \beta)$ commonly used in wireless communication models, which captures the fundamental distance-dependent attenuation through body tissues with parameters that can be empirically determined. For the interaction component, we made the simplifying assumption that interaction effects from multiple receivers add up, a reasonable approximation given that our experimental data showed the total path-loss remains relatively stable across different receiver configurations. Each pairwise interaction $L_{int}(i, j)$ is also modeled as a power law $(\gamma d'(i, j)^{\kappa})$ over the inter-receiver distance, maintaining consistency with the distance-decay principle while allowing the interaction strength to be empirically calibrated. This additive decomposition allows us to separately optimize the spatial placement of receivers (through L_{base}) and account for their mutual coupling (through $\sum L_{int}$), while

Table 4: Path-Loss Measurements for Different Receiver Combinations

Configuration	**Receiver Position**	P_1	P_2	P_3	P_4	P_{tot}
R_{x1}	Chest	-17.43	–	–	–	-17.43
R_{x2}	Left side of the waist	–	-19.41	–	–	-19.41
R_{x3}	Left Calf	–	–	-19.41	–	-19.41
R_{x4}	Right Thigh	–	–	–	-19.34	-19.34
$R_{x1} + R_{x2}$	Chest + LW	-18.80	-21.03	–	–	-16.76
$R_{x1} + R_{x3}$	Chest + LC	-18.27	–	-24.12	–	-17.26
$R_{x1} + R_{x4}$	Chest + RT	-19.02	–	–	-24.42	-17.91
$R_{x2} + R_{x3}$	LW + LC	–	-19.90	-23.31	–	-18.26
$R_{x2} + R_{x4}$	RT + LW	–	-19.45	–	-22.74	-17.78
$R_{x3} + R_{x4}$	RT + LC	–	–	-21.67	-20.35	-17.94
$R_{x1} + R_{x2} + R_{x3}$	Chest + LW + LC	-20.10	-22.63	-26.97	–	-17.63
$R_{x1} + R_{x2} + R_{x4}$	Chest + LW + RC	-21.04	-23.74	–	-22.27	-17.44
$R_{x1} + R_{x3} + R_{x4}$	LW + RT + LC	-20.81	–	-24.54	-23.62	-17.91
$R_{x2} + R_{x3} + R_{x4}$	Chest + LW + RT	–	-20.27	-26.74	-24.49	-18.21
$R_{x1} + R_{x2} + R_{x3} + R_{x4}$	Chest + LW + RT + LC	-21.65	-22.45	-27.32	-26.45	-17.78
Configuration	**Receiver Position**	P_5	P_6	P_7	P_8	P_{tot}
R_{x5}	Torso	-17.91	–	–	–	-17.91
R_{x6}	Right Arm	–	-18.53	–	–	-18.53
R_{x7}	Left Thigh	–	–	-19.47	–	-19.47
R_{x8}	Right Calf	–	–	–	-20.38	-20.38
$R_{x5} + R_{x6}$	Torso + RA	-19.43	-21.18	–	–	-17.21
$R_{x5} + R_{x7}$	Torso + LT	-18.98	–	-22.59	–	-17.41
$R_{x5} + R_{x8}$	Torso + RC	-18.76	–	–	-24.55	-17.74
$R_{x6} + R_{x7}$	RA + LT	–	-19.79	-21.27	–	-17.46
$R_{x6} + R_{x8}$	RA + RC	–	-19.45	–	-22.64	-17.75
$R_{x7} + R_{x8}$	LT + RC	–	–	-20.58	-21.77	-18.12
$R_{x5} + R_{x6} + R_{x7}$	Torso + RA + LT	-20.81	-22.63	-23.97	–	-17.50
$R_{x5} + R_{x6} + R_{x8}$	Torso + RA + RC	-20.86	-22.91	–	-25.29	-17.88
$R_{x5} + R_{x7} + R_{x8}$	Torso + LT + RC	-20.93	–	-23.54	-26.62	-18.33
$R_{x6} + R_{x7} + R_{x8}$	LT + RC + RA	–	-21.23	-22.73	-24.73	-17.90
$R_{x5} + R_{x6} + R_{x7} + R_{x8}$	Torso + RC + RA + LT	-21.63	-23.11	-24.51	-29.05	-17.81

keeping the overall model linear in its parameters for efficient regression-based parameter estimation from our experimental data.

Note that both d_i and $d'(i,j)$ must be computed in the context of 3D body with a rather irregular shape. We do this by discretizing the body into a grid and finding the distance in terms of the path between two receivers (Note that the function is symmetric with respect to receivers i and j).

Thus, for any receiver i, the total path-loss is:

$$\begin{aligned} L_{total}(i) &= L_{base}(i) + \sum_{j \neq i} L_{int}(i,j) \\ L_{base}(i) &= \alpha d_i^{\lambda} + \beta \\ L_{int}(i,j) &= \gamma d'(i,j)^{\kappa} \end{aligned} \tag{7}$$

We then obtain the values of parameters $\alpha, \beta, \lambda, \gamma, \kappa$ using a regression model over the available data. This yields a simple performance model for path-loss (in dB) as a function of the number of receivers and their locations. We next study the performance of this model.

5.3. Path-Loss Model Performance

The model performance was evaluated through 10-fold cross-validation (Table 5). For each fold, we computed the average absolute error by first calculating individual prediction errors for each receiver's path-loss, then averaging across all receivers. The model demonstrated robust predictive capability, maintaining both training and testing errors below 2 dB across all folds. In the best-performing fold, the maximum errors were 2.85 dB for training and 1.57 dB for validation.

Table 5: 10-Fold Cross-Validation Results

	1	**2**	**3**	**4**	**5**	**6**	**7**	**8**	**9**	**10**
Train. Error (dB)	1.043	1.079	1.084	1.089	1.136	1.099	1.050	1.050	1.044	1.076
Valid. Error (dB)	1.359	1.089	0.986	1.007	0.415	0.850	1.309	1.351	1.288	1.184
Summary Statistics:										
Mean Training Error: 1.075 ± 0.028 dB,					Max Training Error (Best fold): 2.85 dB					
Mean Validation Error: 1.084 ± 0.290 dB,					Max Validation Error (Best fold): 1.57 dB					

The main use of this model is to determine a strategy for deciding which intrabody nodes should connect to receive energy when the energy is being transmitted by the energy supplier node (e.g., a smartwatch). Because of the reduction in energy availability for a receiver when other nodes also receive it, it is not always a good idea for all receivers to try to receive it simultaneously, as we have shown in [14].

6. Retuning Single Transmitter-Receiver Pair

In this section, we focus on the problem of retuning of a single transmitter-receiver pair that is initially operating at peak efficiency. The retuning problem in the context of the entire CDMN is discussed in section 7.

6.1. Proposed Retuning Scheme

The problem of detuning of resonant transceiver pair due to various impacts has been well recognized (see related work in section 2.5), but studied largely in the context of wireless power transfer (WPT) in the air media. However, our solution must cater to several aspects: (a) need to consider intrabody context where simplicity, size, lack of manual access, and need for very low power consumption are crucial, (b) a network as opposed to a single transceiver pair, (c) integrated WPT and communication environment.

6.2. Basic Control Issues

We model the disturbance in the transmission as a perturbation in the capacitance of the transmitter and/or the receiver. According to Eq. 6, mitigating such perturbations means controlling the Q-factor and the resonance frequency (and hence the coupling factor). The control of the capacitance can be easily swapped with that of the inductance; however, a change in inductance is generally more difficult to implement. Controlling the resistor also would not be a

viable option since with resistor control, we can only manage the Q-factor, not the resonant frequency. Capacitance is selected because of its ability to affect both objectives: achieving a high Q-factor and resonance. For controller design, we exploit the fact that the current in N_R circuit goes down whenever the two circuits do not resonate, as seen in Fig. 2. Hence, the key part of the controller is to find out which side of the resonance curve we are on using the received current. The controller is tasked with changing the variable controller to achieve resonance. Fig. 8 shows a single energy transmit and receive node pair, denoted as N_T and N_R respectively. We assume a bidirectional communication path and hence the data can flow from N_R to N_T and back.

One important issue in controller design is whether the control algorithm should run on only one side (i.e., at the transmitter or receiver) or on both sides. Since a one-sided retuning is simpler and would be more energy efficient, we implemented a controller on N_T side to manage perturbations on both N_T and N_R sides and discussed the results in section 6.5.2.

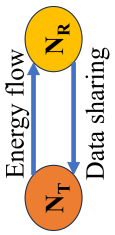

Fig. 8: System Illustration

Another issue is the amount of capacitance change applied by the controller in each step. The simplest approach uses a fixed step-size (FS) in changing the capacitance to achieve resonance. This can be very slow and possibly oscillatory, but computationally efficient. However, since system drift can vary significantly, an adaptive step-size (AS) strategy can be more effective. This approach enables the controller to take larger steps when errors are large and smaller steps when errors are small. To maintain simplicity while preserving adaptability, we limit the controller to three predetermined step sizes rather than allowing arbitrary adjustment. We discussed the results in section 6.5.3.

6.3. Design of the controller algorithm

Let $t = 1, 2, ...$ denote the time instants when the samples are taken. Let C_t and I_t denote the capacitance and the receiver current at time t, respectively. We then construct a truth table for the controller's behavior based on the following equations:

$$\delta = \text{Sign}(C_t - C_{t-1}), \qquad \Delta_I = \text{Sign}(I_t - I_{t-1}) \tag{8}$$

Where Sign() is the sign function. The first equation in 8 describes the direction of capacitance change between t and $t-1$. Similarly, the second equation in 8 describes the direction of current change. Note that the controller acts at time t (the output of the algorithm is C_{t+1}) by tracking the auxiliary states described in the above equations. We should mention that by C_t, we mean the variable capacitance value, which is not affected by the drifting, and only changed by controller actions.

Our control algorithm is described in Alg. 1 and it generalizes the control algorithm described in [60]. The parameters used by the Alg. 1 are listed in Table 5. It is important to note that we recognize the error e_t only when the induced receiver current I_t is less than the reference value I_{ref}. This can be

termed as **Rectified Error Measure** and is the essential difference from the single-link retuning controller described in our earlier work [60]. In that work we used the **Absolute Error Measure**, i.e., $e_t = |I_t - I_{ref}|$. For the single link case discussed in this section, both rectified and absolute versions work almost the same; however, this simple change has profound consequences for the network-wide retuning discussed in section 7.

Symbol	Name	Description
I_t	Current	Induced current at time t
C_t	Capacitance	Capacitance at time t
δ	Capacitance change direction	Sign$(C_t - C_{t-1})$
Δ_I	Current change direction	Sign$(I_t - I_{t-1})$
α	Control direction	The direction of adjustment to increase current
Δ	Step-size	Basic step size for changing the capacitance to achieve resonance
ϵ	Activation threshold	Tolerance of the controller
W'	Weight	Used to weight the first control signal of the controller
W	Initialization weight	Used to shrink the control signals after the initialization
γ	Control scaler	Used to increase the step sizes according to the size of the error e_t
t'	Controller time counter	Time counter that starts when the controller starts and ends with the controller's turn ends
T	Turn duration	Maximum number of controller steps
ϵ' and ϵ''	Moderate and large error thresholds	Error thresholds that control how strongly the system reacts as the error e_t gets larger

Table 5: Controller parameters

The controller operates in discrete intervals, called turns, where it activates, observes the system state, potentially generates a control signal, and then deactivates until the next turn. Each turn consists of up to T time steps, with the controller time counter t' starting from 0 and incrementing by 1 at each step until the turn ends. In each turn, the controller measures the receiver current, computes the error e_t, and uses it to decide on the control action. On the first control step ($t' = 0$), it implements

Alg. 1: Adaptive Step Controller Pseudocode

Observations: I_t, C_t
Parameters: W'; W; ϵ; Δ; α; γ; t'; ϵ'; ϵ''; T
Output: C_{t+1}
Algorithm:
If NOT Controller's Turn **Then** $C_{t+1} \leftarrow C_t, \quad t' = 0$
Else { Measure $I_t(C_t)$, compute $e_t = \max(0, I_{ref} - I_t)$
  If $e_t < \epsilon$ **Then** $C_{t+1} \leftarrow C_t$
  Else {
    if $t' = 0$ (First round) **Then** *Initialization* $C_{t+1} \leftarrow C_t + W'\Delta$
    Else {compute δ, Δ_I
      $\alpha \leftarrow$**Table Look-up**(δ, Δ_I)
      if $\epsilon \le e_t < \epsilon'$ **Then** $C_{t+1} \leftarrow C_t + (W)^{t'} \cdot \alpha \cdot \Delta$
      Else {
        If $\epsilon' \le e_t < \epsilon''$ **Then**
        $C_{t+1} \leftarrow C_t + \gamma(W)^{t'} \cdot \alpha \cdot \Delta$
        Else $C_{t+1} \leftarrow C_t + \gamma^2(W)^{t'} \cdot \alpha \cdot \Delta$
  $t' = t' + 1$
  If $t' \ge T$ **Then** Controller's Turn=False
}}}}

an initial fixed increase ($W'\Delta$) to the capacitance. In subsequent steps, the controller determines the adjustment direction α using Table 6 based on the signs of recent changes in capacitance (δ) and current (Δ_I).

The controller then adjusts the capacitance by a step size that scales with the control step: $(W)^{t'}\Delta$ for moderate errors, or $\gamma(W)^{t'}\Delta$ and $\gamma^2(W)^{t'}\Delta$ for larger errors. This approach systematically moves toward maximizing current and consequently efficiency, until convergence to an ϵ-optimal current is achieved. Since current exhibits unimodal behavior as a function of frequency (as shown in Fig. 2), convergence is guaranteed given sufficiently small step sizes.

Table 6: Capacitance Change Direction as a function of (δ, Δ_I)

δ	+1	+1	-1	-1	-1	-1	+1	+1
Δ_I	+1	+1	-1	-1	+1	+1	-1	-1
α	+1	+1	+1	+1	-1	-1	-1	-1

6.4. Hyperparameters of Control Algorithm

The key hyperparameters of the controller are: *activation threshold* ϵ, *control scaler* γ, *weight* W, and *step size* Δ. The *activation threshold* acts as the convergence criterion: a low activation threshold makes the controller more sensitive to current loss and hence the controller operates more frequently. A high activation threshold makes the controller less responsive to current deviations, potentially missing opportunities for optimization. The selection of this parameter is directly related to the size and form of the perturbation: selecting a small value could lead to reacting to all fluctuations caused by bodily functions during the control interval; selecting a large value could lead to degraded performance, with the controller failing to detect actual problems. *Step size* determines the magnitude of capacitance change at each time step: too large values make the controller oscillatory and unstable, while too small values result in slow convergence with minimal tuning effectiveness. *Control scaler* is used to further adjust the stepping behavior by scaling the step size up or down based on system requirements. *Weight* defines how the step size decreases over successive iterations, implementing a form of adaptive control that helps converge to the optimal values while reducing oscillations as the system approaches equilibrium. Implicitly, the number of steps a controller is allowed to enforce in each turn and the duration of each controller turn are also very important in determining how fast the controller is. That is why for simulations we chose 10 steps per turn, and a 1s period.

Our proposed controller has no exact matching design, but its design borrows from well-known control algorithms. The control drive is closest to Proportional-Derivative (PD) controllers, as its control signal is proportional to the error between measured and reference current, and uses a simple finite difference method to approximate the derivative (since our observations are discrete current measurements) to determine the direction of capacitance adjustment[67]. The weighting mechanism follows adaptive learning rate methods commonly used in gradient-based algorithms[68], while the adaptive step sizing employs a switching control scheme that changes step magnitude based on error thresholds[69].

Essentially, we expect the controller on each side to be able to mirror the disturbances on their respective sides and hence, by reversing the disturbance, diminish their effect.

6.5. Retuning a Transmitter-Receiver Pair

6.5.1. Step vs. Ramp Perturbation and Simulation Setting

We investigated two types of perturbations. The first type is *Step* or glitch, where a 5% change in capacitance happens suddenly but lasts for a short period, following which the capacitance is back to the original value. The second type is a rapid drift or *Ramp* where the capacitance increases linearly until it reaches 5% and then it stays there. For one-sided retuning, we assume only the step perturbation happens on the receiver side. For the one-sided retuning, we consider a particularly challenging case where we assume that (a) the actual change is a combination of the two types, henceforth referred to as Ramp+Step, and (b) the perturbation happens on both transmit and receive sides with a time offset between them. This is shown in Fig. 9. We note that the 5% change is quite large, and chosen merely to illustrate that the controller does work well even for large changes.

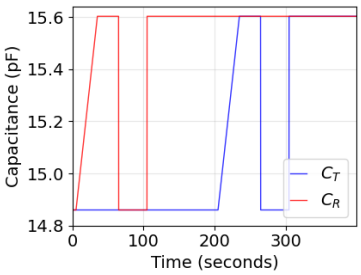

Fig. 9: Capacitance Perturbations

The evaluation was done using simulations in Python, where we simulated the steady state conditions, which, considering an appropriate sampling time, is an appropriate assumption. For the sake of the simulations, we used two variable capacitors in parallel with the initial value of $0.5C$. The capacitance of one of these capacitors is changed according to the perturbation (Drifting Capacitance), and the other one's capacitance changes with the control signal (Control Capacitance). The controller should behave in such a way that the summation of DC and CC would get closer and closer to C, and hence the resonance would be possible. In all the simulations, activation threshold ϵ and step size Δ are set as $1e^{-6}A$ and $2e^{-14}F$ for the fixed step controller. For the adaptive step controller, these parameters are set as $1e^{-6}A$ and $\{5e^{-15}, 2e^{-14}, 8e^{-14}\}F$, respectively ($\gamma = 4$). For both the controllers, W and W' are set as 0.9 and 1, respectively. Also ϵ' and ϵ'' are set to $1e-5$ and $1e-4$. The circuit parameters are set initially as shown in Fig. 3, and the voltage source is set to 1 Volt with the frequency of 13.56 MHz.

6.5.2. One-Sided Retuner

We start by one-sided retuning: the controller resides on N_T, but the 5% step perturbation is on N_R. Table 7 shows the performance of one-sided retuning by three quantities: I_{out}, induced current (in mA) on the receive side, P_{out}, the output power (in mW) on the receive side, and transmission efficiency. It is seen that the controller is not very effective – the transmission efficiency drops quite a

bit (from 50% to 36.3%) after perturbation, but before control action; however, the controller action recovers only 1.1% of it. The last row in Table 7 shows the best case scenario for the controller, i.e., the ability of a hand-crafted (rather than automated) controller. Clearly, hand-crafting hardly makes a difference, meaning that the problem does not lie in the control action per se, but in the handicap of one-sided retuning.

Table 7: Performance with receive side perturbation and transmit side control

Case	I_{out}(mA)	P_{out}(mW)	Eff.
Original unperturbed value	9.99	4.99	50.0%
5% change, Before control action	9.35	4.37	36.3%
5% change, After control	9.75	4.74	37.4%
5% change, Maximum achievable	9.76	4.77	37.5%

6.5.3. Two-Sided Retuner

Because of the deficiency of one-sided retuning shown in Table 7, we henceforth consider only 2-sided control. With two concurrent controllers, each of them acts according to three data flows it receives: current and action at time t and $t-1$. For N_R, it is a matter of recording the data it has already observed, and for N_T, this data is received from N_R. Both N_R and N_T then use Alg.1 according to their turns to calculate the steps they need to take. The two controllers avoid mutual interference between them by giving each a time slot for its turn.

Ramp+Step: This scenario implements the ramp scenario with an additional 5% short-term step occurring once on N_T and once on N_R, and the performance of FS and AS controllers can be seen in Fig. 10. Both controllers achieved over 49% efficiency, recovered over 99% of the maximum power, and settled within 0.9% of the desired capacitance. Comparing the capacitance trajectory and efficiency of FS in Figs. 10a and 10b with AS in Figs. 10d and 10e, the behavior of FS is more erratic (and slower in some cases) due to its dependence on a single step size. AS, on the other hand, is more stable and faster in response. Fig. 11 shows how the control capacitance tries to mirror the trajectory of the perturbed capacitance of the receiver.

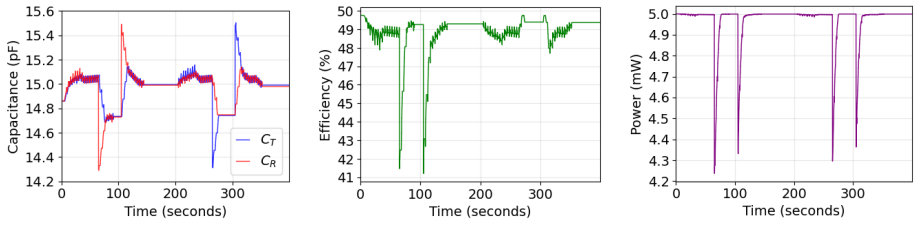

(a) Capacitance Trajectory (b) Efficiency (c) Received Power

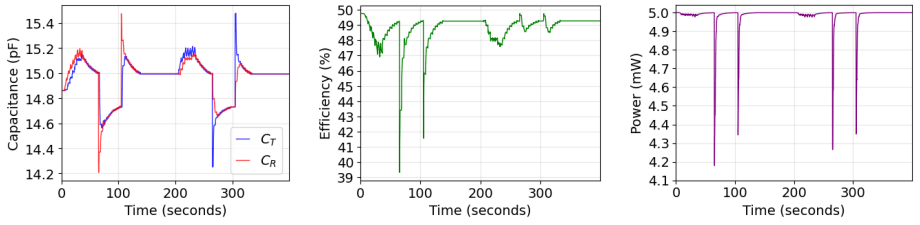

(d) Capacitance Trajectory (e) Efficiency (f) Received Power

Fig. 10: **Performance of Controllers in Ramp+Step Scenario**: Up) Fixed Step; Down) Adaptive Step

The proposed Adaptive Step (AS) controller performs better than the Fixed Step (FS) controller since it has more freedom in choosing how aggressively it can behave. The sharp drops observed in efficiency and power occur because the perturbation caused by the step disturbance pushes the circuit off resonance sharply. However, the controller can bring it back to a near-optimal state. It can also be noted that such drops are not experienced during the ramp disturbance, as the mechanism can compensate for slow changes

The controller can balance the capacitors very quickly. The convergence speed depends mainly on the step size, controller timing, and indirectly on the activation threshold ϵ. However, speed acts as an adversary to the energy efficiency of the controller, and this trade-off should be studied before implementation.

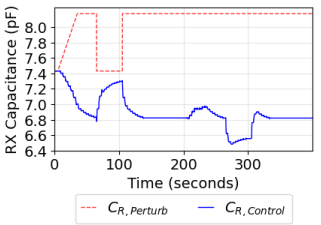

Fig. 11: N_R Capacitance Behavior in Ramp+Step

One interesting observation about the difference between Fixed and Adaptive controllers is their behavior in finding the capacitance value corresponding to maximum power transfer. The Fixed controller behaves erratically even after reaching the optimal value and, as a result, may not converge. This occurs because the fixed step size may cause the controller to overshoot the optimal value, leading both controllers to oscillate around a target that is not reachable with that step size. In contrast, the Adaptive controller can adjust its step size, allowing it to settle at a near-optimal value.

7. Network-wide Retuning

We now focus on the retuning problem in the network setting for a cluster-based network architecture shown in Fig. 1. We propose two methods to address the detuning: (a) a table-driven two-sided retuning appropriate for correlated detuning within a cluster, and (b) a more general but one-sided retuning.

7.1. Table Driven Resonance Frequency Switching

When detuning afflicts CDMN, it is reasonable to expect a similar drifting pattern, both in direction and magnitude, across the entire cluster, likely all clusters. This is because the environmental, mechanical, and physiological factors affect clustered nodes uniformly due to their proximity. The primary challenge with link-by-link tuning approaches is their potential to introduce system instability when components are adjusted individually. To address this, we propose adaptive tuning strategies that operate during successive time periods, with controllers activating sequentially within designated time slots.

In this approach, network hubs maintain lookup tables containing optimal resonance frequencies for each connected sensor. Instead of trying to correct the resonance frequency of sensors to match the hub, hubs dynamically switch their own frequencies to match transmitter-side communications, thereby minimizing signal loss. The adaptive local scheduling reduces the overhead of frequency transitions. However, this method has limitations within current network hierarchies where hubs transmit simultaneously to multiple sensors. The effectiveness of resonance frequency switching depends heavily on cluster optimization strategies. When nodes are densely packed, uniform drifting patterns may maintain consistent optimal frequencies across the cluster. However, this approach might not be energy-efficient, since the hub needs to estimate the optimal frequency of the sensors in a very small period of communication.

7.2. One-Sided Network Retuning

Since the OBN is positioned externally on the body surface and is relatively energy rich, it is possible to use an automated capacitive adjustment (using voltage voltage-controlled capacitor) so that it always maintains its resonance frequency at the design value (e.g., 13.56MHz). This creates a stable frequency reference and thus allows other nodes to autonomously tune themselves to the same frequency and maintain resonance. That is, a one-sided retuning at each sensor/hub node is now adequate. We assume that the retuning work during the energy transfer periods, which have relatively long durations to allow for convergence. However, such a design faces one challenge: The coupling between various receivers due to the complex body media. Consequently, retuning must operate sequentially rather than simultaneously to avoid interference.

Fig. 12 presents a cartoon depicting the control sequence following a drift event under the rectified error measure. We use a color gradient from yellow (lowest current) to dark green (highest current) to indicate receiver current levels. When R_1 drifts (yellow), R_2 and R_3 receive higher currents (dark green) through redistribution. Since the absolute error function only activates when

the current is below the reference, R_2 and R_3 controllers remain inactive and pass without adjustment. Eventually, R_1 corrects itself, resulting in all receivers properly tuned.

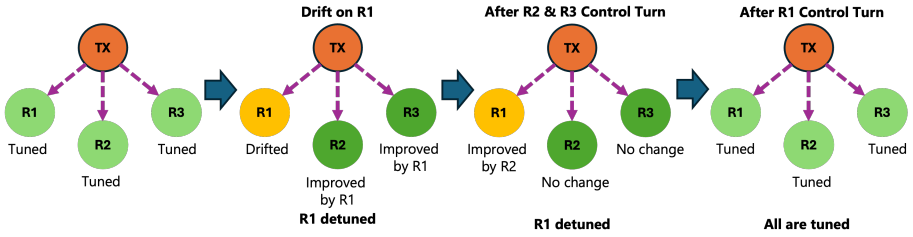

Fig. 12: Effect of Rectified Error Measure

In the following, we study this case for the case of four receivers, with identical circuit parameters and coupling factors as in the previous subsection, to establish a controlled baseline for evaluating the proposed control strategy. We model disturbances as a 5% capacitance increase as a saturated ramp starting for receivers 1 to 4 at 5s, 30s, 55s, and 80s and reaching the 5% after 20s, simulating short-term drift scenarios that might occur due to environmental factors or tissue movement in biomedical applications. With aging-related very slow drifts, the shown undulations will be far smaller and thus not interesting. Each controller acts for 10 seconds, corresponding to 10 control actions, with a minimum step size of 0.004 pF (or 0.027% of the capacitance of 14.86pF) and the control scaler of 5. The sequential timing ensures that only one controller operates at any given time, preventing the interference issues identified with simultaneous control.

7.3. Performance of Rectified Error Retuning

Fig. 13 demonstrates the capacitance trajectory, received power, and efficiency for each receiver. Fig. 13a describes the capacitance trajectories and reveals the key behavior of the rectified error retuning: controller 1 is the only controller that reacts to the receiver 1 perturbation at $t = 5$s, since the other receivers experience a higher than reference current due to energy redistribution from the detuned receiver. When perturbation 2 starts on receiver 2 at $t = 30$s, its current decreases below the reference threshold, activating its controller, and so on for the remaining controllers at subsequent intervals. The flat plateaus in the capacitance trajectories correspond to periods when these receivers are inactive since their currents increase due to the corrective actions of other active controllers, keeping them above the activation threshold.

Fig. 13b shows the efficiency improvement achieved by each retuner during its active periods. The step-wise recovery pattern demonstrates successful perturbation correction, with each receiver returning to near-optimal efficiency levels after its activation. Notably, the efficiency profiles show minimal interference between controllers, validating the control approach.

Fig. 13c illustrates the power redistribution dynamics inherent to coupled wireless power transfer systems. As one receiver becomes detuned, the received power increases in the remaining receivers due to the reduced loading effect of the perturbed receiver. This power redistribution is a natural consequence of the electromagnetic coupling and explains why unperturbed receivers experience higher than reference currents, appropriately deactivating their controllers under the rectified linear activation condition.

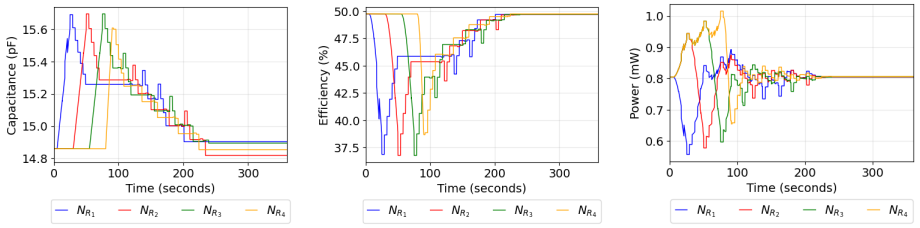

(a) Capacitance Trajectory (b) Efficiency (c) Received Power

Fig. 13: Performance of Control Algorithm

By deactivating the retuners on circuits experiencing increased current, the rectified error retuner for a receiver prevents interference from retuners on other receivers that should remain inactive. This approach recognizes that temporary current increases in unperturbed receivers are beneficial system responses that should not be counteracted. The rectified error retuner thus provides a more dead zone that respects the natural coupling dynamics of the wireless power transfer network.

7.4. Performance of Absolute Error Retuning

In this section, we experimentally show why defining $e_t = |I_t - I_{ref}|$ does not work in the network context. When a receiver becomes detuned, its current decreases while the received currents of the remaining receivers increase due to the redistributed energy in the coupled network. The fundamental issue with the error function is that it triggers controllers on both sides of the reference point: circuits with currents below the reference current (which need tuning) and circuits with currents above the reference current (which are temporarily benefiting from other circuits' detuning). This creates a problematic feedback loop where multiple controllers attempt simultaneous corrections. This problem is depicted in Fig. 12: When R_1 drifts, R_2 and R_3 similarly receive higher currents. However, R_2's controller now activates because any deviation from the reference is treated as an error. R_2 detunes itself to reduce current back to reference, improving R_1 but causing R_3 to receive excess current. R_3 then detunes itself to correct its elevated current. This cascade results in all receivers being detuned despite the system's natural beneficial current redistribution.

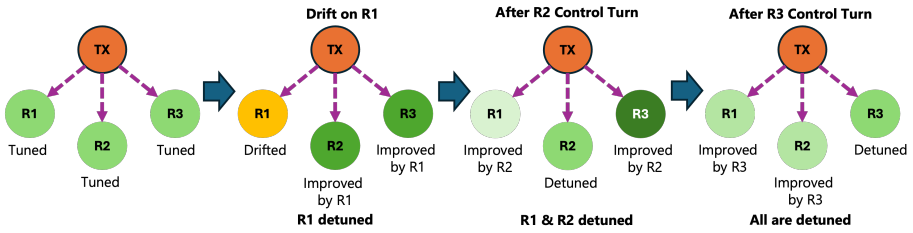

Fig. 14: Effect of Absolute Error Measure

This is demonstrated by the results in Fig. 15. As shown in Fig.15a, the capacitance trajectories exhibit persistent oscillations rather than convergence. The controllers on receivers experience increased current, actively work against the natural energy redistribution, creating conflicting control actions that prevent system stabilization. Furthermore, Fig.15b shows that efficiency continuously fluctuates without reaching steady-state values, indicating the system's inability to find an equilibrium point. While the control scheme can still achieve stability with proper hyperparameter selection, it remains prone to instability.

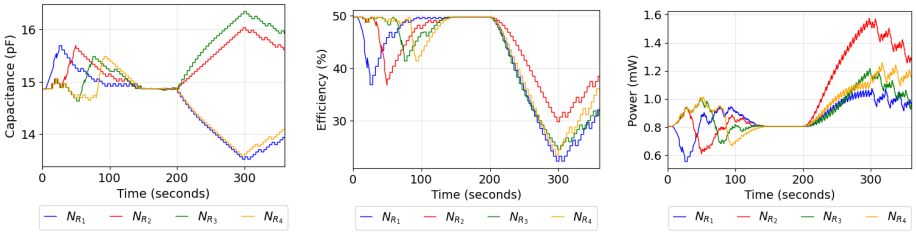

(a) Capacitance Trajectory (b) Efficiency (c) Received Power

Fig. 15: Absolute Error Measure

The energy transfer in a multi-receiver network can be modeled as a competitive game where each receiver seeks to maximize its own power extraction. The error function $|I_t - I_{ref}|$ maintains this competitive dynamic, as controllers continuously attempt to reach their individual reference currents regardless of system-wide effects. In contrast, the rectified error measure $\max(0, I_{ref} - I_t)$ transforms this into a cooperative framework, where receivers cease active control once they achieve their minimum required current, thereby allowing excess energy to benefit other nodes in the network.

8. Conclusions and Discussions

In conclusion, this paper presents a comprehensive characterization of magnetic resonance coupling (MRC) based TTB communications in the context of chronic disease management networks (CDMN). We have demonstrated that MRC propagation through the human body exhibits fundamentally different

characteristics compared to air media, revealing counterintuitive behaviors including frequency-dependent "sweet spots", slow signal attenuation as a function of distance, and insensitivity to relative orientations of transmit and receive antennas. These characteristics deviate substantially from classical near-field predictions. We characterized and modeled the broadcast channel behavior with multiple simultaneous receivers, developing an empirical path-loss model that achieves prediction accuracy within 1 dB and enables systematic energy delivery strategies for battery-less implanted networks. Our retuning mechanism with adaptive step sizing successfully maintains near-optimal efficiency under substantial perturbations in both single-link and network-wide retuning. The presented framework addresses some of the real-world deployment challenges for long-term intrabody medical devices, ensuring sustained performance over the patient's lifetime without requiring invasive maintenance procedures.

In the single transmitter-receiver case, the main assumption is that the observable state for both controllers is the received current. That is, the controller schedule includes the communication back from N_R to N_T, which is a reasonable assumption since the control is necessary only when there is communication happening. In this setting, it is reasonable to assume that the controllers on N_R and N_T are working on the same clock. However, since there is a scheduled communication and controller operation, the controllers are always working according to the schedule and each other; hence, this assumption can be easily removed. An extension to our controller could be a hyper-parameter tuning scheme inside the control loop targeting the control scaler γ according to how much improvement is obtained after each action. Implementing such a retuning scheme could potentially improve the controller's performance when encountering severe disturbances. It is also possible to replace the adaptive step scheme with a continuous function that relates the current deviation to the base step size, directly scaling the steps and totally removing the need for the control scaler; however, with additional overhead. Also, it should be mentioned that Alg. 1 is a three-step controller; it could easily use more or fewer steps. In the context of intrabody energy transfer, severe perturbations are not expected, and more than 3 steps would be an overkill.

The one-sided network retuning approach demonstrates effectiveness because nodes achieve maximum efficiency only when tuned to optimal frequencies, creating a clear performance incentive for maintaining proper resonance. The sequential control strategy prevents the interference issues observed with simultaneous operation while allowing each receiver to respond appropriately to network-wide perturbations. Since the control is implemented only on the receivers participating in energy transfer, we can enhance this strategy by segmenting the energy transfer interval into multiple shorter periods, increasing communication opportunities between nodes, and expanding network coverage across the entire system.

The primary coverage challenge occurs when clustered nodes experience frequency drift, but subsequent energy transfer targets only some of the nodes. This creates problematic frequency mismatches between the tuned and untuned nodes within the same cluster. One possible solution involves intelligently parti-

tioning energy transfer duration to include dedicated communication and tuning phases with all of the nodes, ensuring comprehensive tuning coverage throughout the network topology. However, the trade-off would be the reduced energy transfer efficiency.

It should be emphasized that there is little reason to run the controller during every energy transfer cycle. Instead, sporadic activation provides sufficient drift correction while minimizing system computational overhead, energy consumption, and potential interference with normal network operations. This selective activation strategy balances performance optimization with practical implementation constraints in resource-limited biomedical devices.

As mentioned, the controllers on the nodes are able to converge and stabilize the capacitance values close to that of the OBN, effectively retuning each node to match the OBN's impedance. Once retuning is complete, the nodes can begin communication. The maximum observed post-convergence deviation from the OBN capacitance was 0.8%. In the worst-case scenario with two nodes, this results in a total mismatch of up to 1.6% (relative to the original capacitance). Such a small difference has minimal impact on efficiency (about 3% decrease) and is considered acceptable.

While our experimental work relies primarily on on-body measurements and simulations, and our physiological disturbance modeling makes simplifying assumptions about circuit parameter variations, this work provides essential foundations for practical intrabody communication networks that can operate reliably throughout a patient's lifetime, moving the field significantly closer to realizing permanent, maintenance-free implanted medical device networks capable of addressing the growing global burden of chronic diseases.

Acknowledgments

The project was supported by the National Science Foundation (NSF) grants CNS-2129659. The authors would like to acknowledge considerable amount of measurement and simulation work done by Rajpreet K. Gulati for both MRC and USC technologies originally, and several of those results are included in this paper. The authors would also like to thank Izaz Ali (Hanyang University, Korea) for his help in obtaining Sim4Life results.

References

[1] W. H. Organization, World report on aging, `https://apps.who.int/iris/bitstream/handle/10665/186463/9789240694811_eng.p\protect\discretionary{\char\hyphenchar\font}{}{}df`, 2015.

[2] G. Yang, L. Xie, M. Mäntysalo, X. Zhou, Z. Pang, L. Da Xu, S. Kao-Walter, Q. Chen, L.-R. Zheng, A health-iot platform based on the integration of intelligent packaging, unobtrusive bio-sensor, and intelligent medicine box, IEEE transactions on industrial informatics 10 (2014) 2180–2191.

[3] L. P. Fried, America's health and health care depend on preventing chronic disease, `https://www.huffingtonpost.com/`

entry/americas-health-and-healthcare-depends-on-preventing_us_58c0649de4b070e55af9eade, 2017.

[4] A. Tinker, How to improve patient outcomes for chronic diseases and comorbidities, http://www.healthcatalyst.com/wp-content/uploads/2014/04/How-to-Improve-Patient-Outcomes.pdf, 2017.

[5] United Nations Department of Economic and Social Affairs, World population ageing 2020, 2020. URL: https://www.un.org/en/development/desa/population/publications/pdf/ageing/WorldPopulationAgeing2020-Report.pdf.

[6] H. Y. Tung, K. F. Tsang, H. C. Tung, K. T. Chui, H. R. Chi, The design of dual radio zigbee homecare gateway for remote patient monitoring, IEEE Transactions on Consumer Electronics 59 (2013) 756–764.

[7] H. Tung, K. Tsang, K. Lam, B. Li, L. Yeung, K. Ko, W. Lau, V. Rakocevic, A mobility enabled inpatient monitoring system using a zigbee medical sensor network, Sensors 14 (2014) 2397–2416.

[8] C. Powell, Conditional electrical stimulation in animal and human models for neurogenic bladder: working toward a neuroprosthesis, Current bladder dysfunction reports 11 (2016) 379–385.

[9] T. M. Bruns, N. Bhadra, K. J. Gustafson, Bursting stimulation of proximal urethral afferents improves bladder pressures and voiding, Journal of neural engineering 6 (2009) 066006.

[10] A. Mendez, M. Sawan, T. Minagawa, J.-J. Wyndaele, Estimation of bladder volume from afferent neural activity, IEEE Transactions on Neural Systems and Rehabilitation Engineering 21 (2013) 704–715.

[11] R. G. HAUSER, Techniques for improving cardiac performance with implantable devices, Pacing and Clinical Electrophysiology 7 (1984) 1234–1239.

[12] K. Kaszala, K. A. Ellenbogen, Device sensing: sensors and algorithms for pacemakers and implantable cardioverter defibrillators, Circulation 122 (2010) 1328–1340.

[13] R. A. Normann, E. Fernandez, Clinical applications of penetrating neural interfaces and utah electrode array technologies, Journal of neural engineering 13 (2016) 061003.

[14] H. Kia, P. Pandit, K. Kant, Energy transfer strategies in magnetic resonance based intrabody networks, Proc. WoWMoM conf., Available at https://www.kkant.net/Hirsa_CDMN_energy_paper.pdf (2025).

[15] P. Pandit, H. Kia, K. Kant, Energy efficiency and communication accuracy tradeoff in intra-body networks, in: Proc. of ACM CHASE conf., Available at https://www.kkant.net/Pramita_CDMN_comm_paper.pdf, ACM, New York, NY, USA, 2025. doi:10.1145/3721201.3721411.

[16] M. Abrams, Near field magnetic induction (nfmi): Dreams of wireless hearables, http://www.audioxpress.com/article/near-field-magnetic-induction-nfmi-dreams-of-wireless-hearables, 2017.

[17] E. Wen, D. F. Sievenpiper, P. P. Mercier, Channel characterization of magnetic human body communication, IEEE Transactions on Biomedical Engineering 69 (2021) 569–579.

[18] R. Shukla, N. Kiran, R. Wang, J. Gummeson, S. Lee, Skinnypower: enabling batteryless wearable sensors via intra-body power transfer, Proceedings of the 17th Conference on Embedded Networked Sensor Systems (2019).

[19] A. Pal, K. Kant, Nfmi: Near field magnetic induction basedcommunication, Elsevier Computer Networks (2020). doi:10.1016/j.comnet.2020.107548.

[20] J. I. Agbinya, Principles of Inductive Near Field Communications for Internet of Things, River Publishers, Wharton, TX, USA, 2011.

[21] M. Masihpour, Cooperative communication in near field magnetic induction communication systems, Ph.D. thesis, University of Technology, Sydney, 2012.

[22] J. Van Mulders, D. Delabie, C. Lecluyse, C. Buyle, G. Callebaut, L. Van der Perre, L. De Strycker, Wireless power transfer: Systems, circuits, standards, and use cases, Sensors 22 (2022) 5573.

[23] S. Islam, R. K. Gulati, M. Domic, A. Pal, K. Kant, A. Kim, Performance evaluation of magnetic resonance coupling method for intra-body network (ibnet), IEEE Transactions on Biomedical Engineering 69 (2022) 1901–1908. doi:10.1109/TBME.2021.3130408.

[24] R. K. Gulati, S. Islam, A. Pal, K. Kant, A. Kim, Characterization of magnetic communication through human body, IEEE Consumer Communications and Networking Conference (CCNC) (2022) 563–568. doi:10.1109/CCNC49033.2022.9700669.

[25] S. Gabriel, R. Lau, C. Gabriel, The dielectric properties of biological tissues: Ii. measurements in the frequency range 10 hz to 20 ghz, Physics in medicine & biology 41 (1996) 2251.

[26] N. Siauve, R. Scorretti, N. Burais, L. Nicolas, A. Nicolas, Electromagnetic fields and human body: a new challenge for the electromagnetic field computation, COMPEL 22 (2003) 457–469.

[27] D. Andreuccetti, R. Fossi, Proprietà dielettriche dei tessuti umani: definizioni, modello parametrico, codici di calcolo., http://niremf.ifac.cnr.it/tissprop/, 2000.

[28] I. Poole, Understanding ceramic capacitors and its types, www.electronics-notes.com, n.d.

[29] N. Jiang, L. Zhang, Z.-Q. Liu, L. Sun, W.-M. Long, P. He, M.-Y. Xiong, M. Zhao, Reliability issues of lead-free solder joints in electronic devices, Science and technology of advanced materials 20 (2019) 876–901.

[30] A. Kurs, A. Karalis, R. Moffatt, J. D. Joannopoulos, P. Fisher, M. Soljacic, Wireless power transfer via strongly coupled magnetic resonances, science 317 (2007) 83–86.

[31] M. Kiani, U.-M. Jow, M. Ghovanloo, Design and optimization of a 3-coil inductive link for efficient wireless power transmission, IEEE transactions on biomedical circuits and systems 5 (2011) 579–591.

[32] J. S. Ho, A. J. Yeh, E. Neofytou, S. Kim, Y. Tanabe, B. Patlolla, R. E. Beygui, A. S. Poon, Wireless power transfer to deep-tissue microimplants, Proceedings of the National Academy of Sciences 111 (2014) 7974–7979.

[33] D. Xu, Q. Zhang, X. Li, Implantable magnetic resonance wireless power transfer system based on 3d flexible coils, Sustainability 12 (2020) 4149.

[34] M. K. Hoang, X. T. Kieu, X. T. Pham, T. K. Vu, T. S. Pham, A design of magnetic resonant wireless power transfer system using flexible resonator coils, Journal of Magnetics 28 (2023) 323–330.

[35] H. K. Abduljaleel, S. K. Gharghan, A. J. A. Al-Gburi, Multi-layer square coil-based wireless power transfer for biomedical implants., Progress in Electromagnetics Research B 111 (2025).

[36] L. Kouhalvandi, S. Ozoguz, M. Koohestani, A literature survey with the focus on magnetically coupled wireless power transfer systems developed for engineering and biomedical applications, Micromachines 14 (2023) 786.

[37] S. Ozeri, D. Shmilovitz, Ultrasonic transcutaneous energy transfer for powering implanted devices, Ultrasonics 50 (2010) 556–566.

[38] A. Kim, S. K. Lee, T. Parupudi, R. Rahimi, P. chul, Moon, Islam, Sayemul, Zhou, Jiawei, Majumdar, A. K., Park, J. S., Yoo, J. M., Ziaie, B., An Ultrasonically Powered Implantable Microprobe for Electrolytic Ablation, Scientific Reports Under review (2019).

[39] T. C. Chang, M. J. Weber, M. L. Wang, J. Charthad, B. P. T. Khuri-Yakub, A. Arbabian, Design of Tunable Ultrasonic Receivers for Efficient Powering of Implantable Medical Devices With Reconfigurable Power Loads, IEEE Transactions on Ultrasonics, Ferroelectrics, and Frequency Control 63 (2016) 1554–1562. doi:10.1109/TUFFC.2016.2606655.

[40] D. Seo, R. M. Neely, K. Shen, U. Singhal, E. Alon, J. M. Rabaey, J. M. Carmena, M. M. Maharbiz, Wireless recording in the peripheral nervous system with ultrasonic neural dust, Neuron 91 (2016) 529–539.

[41] M. J. Weber, Y. Yoshihara, A. Sawaby, J. Charthad, T. C. Chang, A. Arbabian, A miniaturized single-transducer implantable pressure sensor with time-multiplexed ultrasonic data and power links, IEEE Journal of Solid-State Circuits 53 (2018) 1089–1101.

[42] J. Charthad, T. C. Chang, Z. Liu, A. Sawaby, M. J. Weber, S. Baker, F. Gore, S. A. Felt, A. Arbabian, A mm-sized wireless implantable device for electrical stimulation of peripheral nerves, IEEE transactions on biomedical circuits and systems 12 (2018) 257–270.

[43] Q. Wang, Y. Zhang, H. Xue, Y. Zeng, G. Lu, H. Fan, L. Jiang, J. Wu, Lead-free dual-frequency ultrasound implants for wireless, biphasic deep brain stimulation, Nature communications 15 (2024) 4017.

[44] A. Ibrahim, M. Meng, M. Kiani, A comprehensive comparative study on inductive and ultrasonic wireless power transmission to biomedical implants, IEEE sensors journal 18 (2018) 3813–3826.

[45] B. L. Cannon, J. F. Hoburg, D. D. Stancil, S. C. Goldstein, Magnetic resonant coupling as a potential means for wireless power transfer to multiple small receivers, IEEE Transactions on Power Electronics 24 (2009) 1819–1825. doi:10.1109/TPEL.2009.2017195.

[46] K. Zhang, C. Liu, Z. H. Jiang, Y. Zhang, X. Liu, H. Guo, X. Yang, Near-field wireless power transfer to deep-tissue implants for biomedical applications, IEEE Transactions on Antennas and Propagation 68 (2019) 1098–1106.

[47] S.-Y. Lee, C.-Y. Huang, Bladder control implants, in: Handbook of Biochips: Integrated Circuits and Systems for Biology and Medicine, Springer, 2022, pp. 3–20.

[48] Ting Chia Chang, M. Weber, J. Charthad, A. Nikoozadeh, P. T. Khuri-Yakub, A. Arbabian, Design of high-efficiency miniaturized ultrasonic receivers for powering medical implants with reconfigurable power levels, in: 2015 IEEE International Ultrasonics Symposium (IUS), IEEE, Taipei, Taiwan, 2015, pp. 1–4. URL: http://ieeexplore.ieee.org/document/7329613/. doi:10.1109/ULTSYM.2015.0215.

[49] S. R. Khan, S. K. Pavuluri, G. Cummins, M. P. Y. Desmulliez, Wireless Power Transfer Techniques for Implantable Medical Devices: A Review, Sensors 20 (2020) 3487. URL: https://www.mdpi.com/1424-8220/20/12/3487. doi:10.3390/s20123487.

[50] P. Si, A. P. Hu, S. Malpas, D. Budgett, A frequency control method for regulating wireless power to implantable devices, IEEE transactions on biomedical circuits and systems 2 (2008) 22–29.

[51] Y. Lim, H. Tang, S. Lim, J. Park, An adaptive impedance-matching network based on a novel capacitor matrix for wireless power transfer, IEEE Transactions on Power Electronics 29 (2013) 4403–4413.

[52] R. W. Porto, V. J. Brusamarello, L. A. Pereira, F. R. de Sousa, Fine tuning of an inductive link through a voltage-controlled capacitance, IEEE Transactions on Power Electronics 32 (2016) 4115–4124.

[53] W. Li, G. Wei, C. Cui, X. Zhang, Q. Zhang, A double-side self-tuning lcc/s system using a variable switched capacitor based on parameter recognition, IEEE Transactions on Industrial Electronics 68 (2020) 3069–3078.

[54] J. Tian, A. P. Hu, Adjusting the frequency of an autonomous push pull converter for wireless power transfer by varying the equivalent resonant capacitance through balanced dc voltage control, in: 2015 IEEE PELS Workshop on Emerging Technologies: Wireless Power (2015 WoW), IEEE, 2015, pp. 1–4.

[55] A. Namadmalan, Self-oscillating tuning loops for series resonant inductive power transfer systems, IEEE Transactions on Power Electronics 31 (2015) 7320–7327.

[56] R. Mai, Y. Liu, Y. Li, P. Yue, G. Cao, Z. He, An active-rectifier-based maximum efficiency tracking method using an additional measurement coil for wireless power transfer, IEEE Transactions on Power Electronics 33 (2017) 716–728.

[57] R. Gulati, K. Kant, A. Pal, Ultrasonic vs. magnetic resonance communication for mixed wearable and implanted devices, Proc. of IEEE International Conf. on Communications (ICC) (2022) 5304–5309. doi:10.1109/ICC45855.2022.9838598.

[58] F. Akasheh, T. Myers, J. D. Fraser, S. Bose, A. Bandyopadhyay, Development of piezoelectric micromachined ultrasonic transducers, Sensors and Actuators A: Physical 111 (2004) 275–287.

[59] H. Kia, R. Gulati, K. Kant, A study of magnetic resonance and ultrasound based through-the-body communications, Proc. of IEEE WiMob conference (2024). doi:10.1109/WiMob61911.2024.10770313.

[60] H. Kia, K. Kant, Autotuning of resonant magnetic induction communications, Accepted for DCOSS-IoT (Intl. conf. on dist. computing in Smart Systems and IoT), available at https://www.kkant.net/papers/qfactor_tuning.pdf (2024).

[61] G. K. Johnsen, Skin electrical properties and physical aspects of hydration of keratinized tissues (2010).

[62] Ettus Research, a National Instruments Brand, Ettus USRP N210, www.ettus.com/products/un210, 2012.

[63] M. D. Maas, Open-source electromagnetic simulation: Fdtd, fem, mom, https://www.matecdev.com/posts/differences-fdtd-fem-mom.html, 2021.

[64] S. ZMT Zurich MedTech AG, Zurich, Sim4life, https://zmt.swiss/sim4life/, 2023.

[65] K.-W. Yang, K. Oh, S. Ha, Challenges in scaling down of free-floating implantable neural interfaces to millimeter scale, IEEE Access 8 (2020) 133295–133320.

[66] C. Han, L. Kong, Q. Li, S. Yu, Z. Zhang, J. Mao, The wireless power transmission on the wrist-to-forehead path based on the body channel, JOURNAL OF BEIJING INSTITUTE OF TECHNOLOGY 31 (2022) 91–100.

[67] Z. Miao, D. Liu, C. Gong, An adaptive impedance matching network with closed loop control algorithm for inductive wireless power transfer, Sensors 17 (2017) 1759.

[68] K. J. Astrom, B. Wittenmark, Adaptive control, Addison-Wesley Longman Publishing Co., Inc., 1994.

[69] K. S. Narendra, A. M. Annaswamy, Stable adaptive systems, Courier Corporation, 2012.